Magnetic breakdown spectrum of a Kramers–Weyl semimetal

Lemut, G.; Donís Vela, A.; Pacholski, M.J.; Tworzydło, J.; Beenakker, C.W.J.

PAPER • OPEN ACCESS

Magnetic breakdown spectrum of a Kramers–Weyl semimetal

New Journal of Physics
The open access journal at the forefront of physics

Deutsche Physikalische Gesellschaft DPG
IOP Institute of Physics

Published in partnership with: Deutsche Physikalische Gesellschaft and the Institute of Physics

OPEN ACCESS

RECEIVED
22 April 2020

REVISED
29 July 2020

ACCEPTED FOR PUBLICATION
10 August 2020

PUBLISHED
9 September 2020

PAPER

Magnetic breakdown spectrum of a Kramers–Weyl semimetal

G Lemut[1], A Donís Vela[1], M J Pacholski[1], J Tworzydło[2] and C W J Beenakker[1]

[1] Instituut-Lorentz, Universiteit Leiden, P.O. Box 9506, 2300 RA Leiden, The Netherlands
[2] Faculty of Physics, University of Warsaw, ul. Pasteura 5, 02–093 Warszawa, Poland

Keywords: Landau levels, Fermi arcs, Kramers degeneracy, magnetic oscillations

Abstract

We calculate the Landau levels of a Kramers–Weyl semimetal thin slab in a perpendicular magnetic field B. The coupling of Fermi arcs on opposite surfaces broadens the Landau levels with a band width that oscillates periodically in $1/B$. We interpret the spectrum in terms of a one-dimensional superlattice induced by magnetic breakdown at Weyl points. The band width oscillations may be observed as $1/B$-periodic magnetoconductance oscillations, at weaker fields and higher temperatures than the Shubnikov–de Haas oscillations due to Landau level quantization. No such spectrum appears in a generic Weyl semimetal, the Kramers degeneracy at time-reversally invariant momenta is essential.

1. Introduction

Kramers–Weyl fermions are massless low-energy excitations that may appear in the Brillouin zone near time-reversally invariant momenta (TRIM). Their gapless nature is protected by Kramers degeneracy, which enforces a band crossing at the TRIM. Crystals that support Kramers–Weyl fermions have strong spin–orbit coupling and belong to one of the chiral point groups, without reflection or mirror symmetry, to allow for a linear rather than quadratic band splitting away from the TRIM. The materials are called topological chiral crystals or Kramers–Weyl semimetals—to be distinguished from generic Weyl semimetals where Kramers degeneracy plays no role. Several candidates were predicted theoretically [1, 2] and some have been realized in the laboratory [3–7].

These recent developments have motivated the search for observables that would distinguish Kramers–Weyl fermions from generic Weyl fermions [8–10]. Here we report on the fundamentally different Landau level spectrum when the semimetal is confined to a thin slab in a perpendicular magnetic field.

Generically, Landau levels are dispersionless: the energy does not depend on the momentum in the plane perpendicular to the magnetic field B. In contrast, we have found that the Landau levels of a Kramers–Weyl semimetal are broadened into a Landau band. The band width oscillates periodically in $1/B$, producing an oscillatory contribution to the magnetoconductance.

The phenomenology is similar to that encountered in a semiconductor 2D electron gas in a superlattice potential [11–15]. In that system the dispersion is due to the drift velocity of cyclotron orbits in perpendicular electric and magnetic fields. Here the surface Fermi arcs provide for open orbits, connected to closed orbits by magnetic breakdown (MB) at Weyl points (see figure 1).

No open orbits appear in a generic Weyl semimetal [16, 17], because the Weyl points are closely separated inside the first Brillouin zone, so the Fermi arcs are short and do not cross the Brillouin zone boundaries (a prerequisite for open orbits). The Landau band dispersion therefore directly ties into a defining property [1] of a Kramers–Weyl semimetal: surface Fermi arcs that span the entire Brillouin zone because they connect TRIM at zone boundaries.

In the next two sections 2 and 3 we first compute the spectrum of a Kramers–Weyl semimetal slab in zero magnetic field, to obtain the equi-energy contours that govern the orbits when we apply a perpendicular field. The resonant tunneling between open and closed orbits via MB is studied in section 4. With these preparations we are ready to calculate the dispersive Landau bands and the magnetoconductance oscillations in sections 5 and 6. The analytical calculations are then compared with the numerical solution of a tight-binding model in sections 7 and 8. We conclude in section 9.

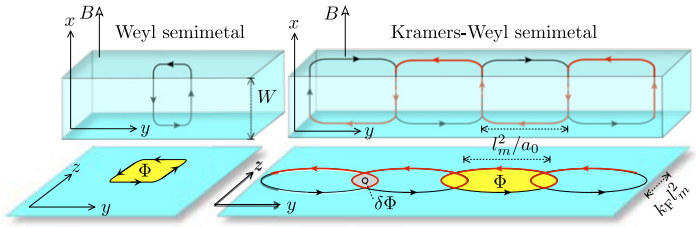

Figure 1. Electron orbits in a thin slab geometry perpendicular to a magnetic field (along the x-axis), for a generic Weyl semimetal [16, 17] (at the left) and for a Kramers–Weyl semimetal (at the right). In each case we show separately a front view (in the x–y plane, to show how the orbits switch between top and bottom surfaces of the slab) and a top view (in the y–z plane, to indicate the magnetic flux enclosed by the orbits). The Kramers–Weyl semimetal combines open orbits (red arrows) with closed orbits enclosing either a large flux Φ or a small flux $\delta\Phi$. Open and closed orbits are coupled by a periodic chain of MB events, spaced by l_m^2/a_0 (with a_0 the lattice constant and $l_m = \sqrt{\hbar/eB}$ the magnetic length). The open orbits broaden the Landau levels into a band, the band width varies from minimal to maximal when $\delta\Phi$ is incremented by h/e. Because $\delta\Phi \propto Bl_m^4 \propto 1/B$, the band width oscillations are periodic in $1/B$.

2. Boundary condition for Kramers–Weyl fermions

The first step in our analysis is to characterize the surface Fermi arcs in a Kramers–Weyl semimetal, which requires a determination of the boundary condition for Kramers–Weyl fermions. This is more strongly constrained by time-reversal symmetry than the familiar boundary condition on the Dirac equation [18]. In that case the confinement by a Dirac mass $V_\mu = \mu\left(\hat{\boldsymbol{n}}_\parallel \cdot \boldsymbol{\sigma}\right)$ generates a boundary condition

$$\Psi = (\hat{\boldsymbol{n}}_\perp \times \hat{\boldsymbol{n}}_\parallel) \cdot \boldsymbol{\sigma}\Psi. \tag{2.1}$$

The unit vectors $\hat{\boldsymbol{n}}_\parallel$ and $\hat{\boldsymbol{n}}_\perp$ are parallel and perpendicular to the boundary, respectively.

Although $\boldsymbol{\sigma} \mapsto -\boldsymbol{\sigma}$ upon time reversal, the Dirac mass may still preserve time-reversal symmetry if the Weyl fermions are not at a time-reversally invariant momentum (TRIM). For example, in graphene a Dirac mass $+\mu$ at the K-point in the Brillouin zone and a Dirac mass $-\mu$ at the K′-point preserves time-reversal symmetry. In contrast, for Kramers–Weyl fermions at a TRIM the V_μ term in the Hamiltonian is incompatible with time-reversal symmetry. To preserve time-reversal symmetry the boundary condition must couple two Weyl cones, it cannot be of the single-cone form (2.1).

In appendix A we demonstrate that, indeed, pairs of Weyl cones at a TRIM are coupled at the boundary of a Kramers–Weyl semimetal. Relying on that result, we derive in this section the time-reversal invariant boundary condition for Kramers–Weyl fermions.

We consider a Kramers–Weyl semimetal in a slab geometry, confined to the y–z plane by boundaries at $x = 0$ and $x = W$. In a minimal description we account for the coupling of two Weyl cones at the boundary. To first order in momentum $\boldsymbol{k}$, measured from a Weyl point, the Hamiltonian of the uncoupled Weyl cones is

$$\begin{aligned} H_\pm(\boldsymbol{k}) &= \begin{pmatrix} H_0(\boldsymbol{k}) + \varepsilon & 0 \\ 0 & \pm H_0(\boldsymbol{k}) - \varepsilon \end{pmatrix}, \\ H_0(\boldsymbol{k}) &= \sum_{\alpha=x,y,z} v_\alpha k_\alpha \sigma_\alpha. \end{aligned} \tag{2.2}$$

The $\pm$ sign indicates whether the two Weyl cones have the same chirality $(+)$ or the opposite chirality $(-)$. The two Weyl points need not be at the same energy, we allow for an offset ε. We also allow for anisotropy in the velocity components v_α.

The σ_α's are Pauli matrices acting on the spin degree of freedom. We will also use τ_α Pauli matrices that act on the Weyl cone index, with σ_0 and τ_0 the corresponding 2×2 unit matrix. We can then write

$$H_+ = H_0\tau_0 + \varepsilon\tau_z, \quad H_- = H_0\tau_z + \varepsilon\tau_z. \tag{2.3}$$

The current operator in the x-direction is $j_+ = v_x\sigma_x\tau_0$ for H_+ and $j_- = v_x\sigma_x\tau_z$ for H_-. The time-reversal operation $\mathcal{T}$ does not couple Weyl cones at a TRIM, it only inverts the spin and momentum:

$$\mathcal{T}H_\pm(\boldsymbol{k})\mathcal{T}^{-1} = \sigma_y H_\pm^*(-\boldsymbol{k})\sigma_y = H_\pm(\boldsymbol{k}). \tag{2.4}$$

An energy-independent boundary condition on the wave function Ψ has the general form [18]

$$\Psi = M_\pm \cdot \Psi, \quad M_\pm = M_\pm^\dagger, \quad M_\pm^2 = 1, \tag{2.5}$$

in terms of a Hermitian and unitary matrix $M_\pm$. The matrix $M_\pm$ anticommutes with the current operator $j_\pm$ perpendicular to the surface, to ensure current conservation. Time-reversal symmetry further requires that

$$\sigma_y M_\pm^* \sigma_y = M_\pm. \tag{2.6}$$

These restrictions reduce $M_\pm$ to the single-parameter form

$$\begin{aligned} M_+(\phi) &= \tau_y\sigma_y \ \cos\ \phi + \tau_y\sigma_z \ \sin\ \phi, \\ M_-(\phi) &= \tau_x\sigma_0 \ \cos\ \phi + \tau_y\sigma_x \ \sin\ \phi. \end{aligned} \tag{2.7}$$

The angle ϕ has a simple physical interpretation in the case H_+, M_+ case of two coupled Weyl cones of the same chirality: it determines the direction of propagation of the helical surface states (the Fermi arcs). We will take $\phi = 0$ at $x = 0$ and $\phi = \pi$ at $x = W$. This produces a surface state that is an eigenstate of $\tau_y\sigma_y$ with eigenvalue $+1$ on one surface and eigenvalue -1 on the opposite surface, so a circulating surface state in the $\pm y$-direction. (Alternatively, if we would take $\phi = \pm\pi/2$ the state would circulate in the $\pm z$-direction.)

Notice that these are helical rather than chiral surface states: the eigenstates Ψ of $\tau_y\sigma_y$ with eigenvalue $+1$ contain both right-movers ($\sigma_y\Psi = +\Psi$) and left-movers ($\sigma_y\Psi = -\Psi$). This is the key distinction with surface states in a magnetic Weyl semimetal, which circulate unidirectionally around the slab [19–22].

In the case H_-, M_- that the coupled Weyl cones have the opposite chirality there are no helical surface states and the physical interpretation of the angle ϕ in equation (2.7) is less obvious. Since our interest here is in the Fermi arcs, we will not consider that case further in what follows.

3. Fermi surface of Kramers–Weyl fermions in a slab

3.1. Dispersion relation

We calculate the energy spectrum of H_+ with boundary condition M_+ from equation (2.7) along the lines of reference [23]. Integration in the x-direction of the wave equation $H_\pm\Psi = E\Psi$ with $k_x = -i\hbar\partial/\partial x$ relates the wave amplitudes at the top and bottom surface via $\Psi(W) = e^{i\Xi}\Psi(0)$, with

$$\Xi = \frac{W}{\hbar v_x}\sigma_x(E - v_y k_y\sigma_y - v_z k_z\sigma_z - \varepsilon\tau_z). \tag{3.1}$$

As discussed in section 2 we impose the boundary condition $\Psi = M_+(0)\Psi$ on the $x = 0$ surface and $\Psi = M_+(\pi)\Psi$ on the $x = W$ surface.

The round-trip evolution

$$\Psi(0) = M_+(0)\mathrm{e}^{-\mathrm{i}\Xi}M_+(\pi)\mathrm{e}^{\mathrm{i}\Xi}\Psi(0) \tag{3.2}$$

then gives the determinantal equation

$$\mathrm{Det}\left(1 + \tau_y\sigma_y\mathrm{e}^{-\mathrm{i}\Xi}\tau_y\sigma_y\mathrm{e}^{\mathrm{i}\Xi}\right) = 0, \tag{3.3}$$

which evaluates to

$$[E^2 - \varepsilon^2 + (v_z k_z)^2 - (v_y k_y)^2]\frac{\sin\ w_-\ \sin\ w_+}{q_- q_+} = 1 + \cos\ w_-\ \cos\ w_+, \tag{3.4}$$

with the definitions

$$q_\pm^2 = (E \pm \varepsilon)^2 - (v_y k_y)^2 - (v_z k_z)^2, \quad w_\pm = \frac{W}{\hbar v_x}q_\pm. \tag{3.5}$$

In the zero-offset limit $\varepsilon = 0$ equation (3.4) reduces to the more compact expression

$$\left(\frac{v_z k_z}{q}\ \tan\ \frac{Wq}{\hbar v_x}\right)^2 = 1, \quad q^2 = E^2 - (v_y k_y)^2 - (v_z k_z)^2, \tag{3.6}$$

which is a squared Weiss equation [23, 24].

The dispersion relation $E(k_y, k_z)$ which follows from equation (3.4) is plotted in figure 2. The surface states (indicated in red) are nearly flat as function of k_z, so they propagate mainly in the $\pm y$ direction. In the limit $\varepsilon \to 0$ the bands cross at $k_z = 0$, this crossing is removed by the energy offset.

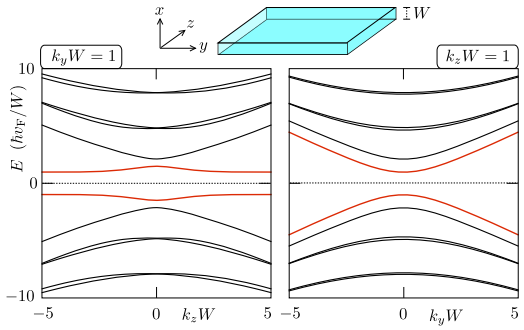

Figure 2. Dispersion relation $E(k_y, k_z)$ as a function of k_z for fixed $k_y = 1/W$ (left panel) and as a function of k_y for fixed $k_z = 1/W$ (right panel), calculated from equation (3.4) for $v_x = v_y = v_z \equiv v_F$ and $\varepsilon = \hbar v_F/W$. The surface states are indicated in red. The avoided crossings at $k_z = 0$ become real crossings for $\varepsilon = 0$.

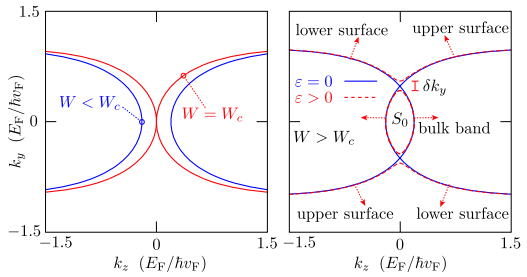

Figure 3. Solid curves: equi-energy contours $E(k_y, k_z) = E_F$ for $\varepsilon = 0$ at three values of W (in units of $\hbar v_F/E_F$ with $E_F > 0$): $W = \pi/2 = W_c$ (red curve in left panel), $W = 1.4 < W_c$ (blue curve in left panel), and $W = 1.8 > W_c$ (blue curve in right panel). The calculations are based on equation (3.4) with $v_x = v_y = v_z \equiv v_F$. The red dashed curve in the right panel shows the effect of a nonzero $\varepsilon = 0.1E_F$: the intersecting contours break up into two open and one closed contour, separated at $k_z = 0$ by a gap δk_y. The dotted arrows, perpendicular to the equi-energy contours, point into the direction of motion in real space. The assignment of the bands to the upper and lower surface is in accord with the time-reversal symmetry requirement that a band stays on the same surface when $(k_y, k_z) \mapsto -(k_y, k_z)$.

3.2. Fermi surface topology

The equi-energy contours $E(k_y, k_z) = E_F$ are plotted in figure 3 for several values of W. The topology of the Fermi surface changes at a critical width

$$W_c = \frac{\pi}{2}\frac{\hbar v_x}{E_F} + \mathcal{O}(\varepsilon). \tag{3.7}$$

At $W = W_c$ the surface bands from upper and lower surface touch at the Weyl point $k_y = k_z = 0$, and for larger widths the upper and lower surface bands decouple from a bulk band, in the interior of the slab.

For $\varepsilon = 0$ the surface and bulk bands intersect at $k_z = 0$ when $W > W_c$. The gap δk_y which opens up for nonzero ε is

$$\delta k_y = \frac{4}{\pi v_y}|\varepsilon| + \mathcal{O}(\varepsilon^2), \quad W > W_c. \tag{3.8}$$

For later use we also record the area S_0 enclosed by the bulk band,

$$S_0 = \frac{4}{3}\pi\sqrt{2}(W/W_c - 1)^{3/2}k_F^2 + \mathcal{O}(W/W_c - 1)^2 + \mathcal{O}(\varepsilon), \tag{3.9}$$

where we have defined the 2D Fermi wave vector of the Weyl fermions via

$$E_F = \hbar k_F\sqrt{v_y v_z}. \tag{3.10}$$

4. Resonant tunneling between open and closed orbits in a magnetic field

Upon application of a magnetic field B in the x-direction, perpendicular to the slab, the Lorentz force causes a wave packet to drift along an equi-energy contour. Because $\dot{\boldsymbol{k}} = e\dot{\boldsymbol{r}} \times \boldsymbol{B}$ the orbit in real space is obtained from the orbit in momentum space by rotation over $\pi/2$ and rescaling by a factor $\hbar/eB = l_m^2$ (magnetic length squared).

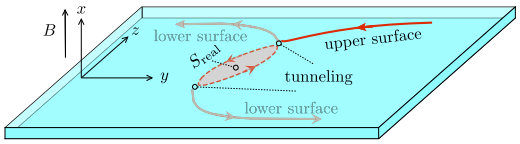

Figure 4. Electron orbits in a magnetic field perpendicular to the slab, following from the Fermi surface in figure 3 ($W > W_c$, $\varepsilon > 0$). The tunneling events (MB) between open and closed orbits are indicated. These happen with probability $T_{\rm MB}$ given by equation (4.1). Backscattering of the open orbit via the closed orbit happens with probability $\mathcal{R}$ given by equation (4.2). The area $S_{\rm real} \propto 1/B^2$ of the closed orbit in real space determines the $1/B$ periodicity of the magnetoconductance oscillations via the resonance condition $BS_{\rm real} = nh/e$.

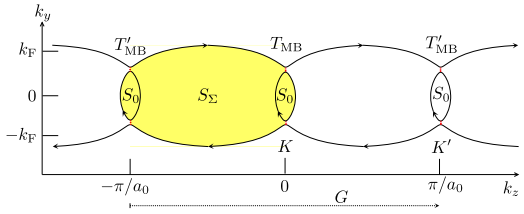

Figure 5. Equi-energy contours in the k_y–k_z plane, showing open orbits coupled to closed orbits via magnetic breakdown (red dotted lines). The closed contours encircle Weyl points at $\boldsymbol{K} = (0, 0)$ and $\boldsymbol{K}' = (0, \pi/a_0)$—periodically translated by the reciprocal lattice vector $\boldsymbol{G} = (0, 2\pi/a_0)$. Arrows indicate the spectral flow in a perpendicular magnetic field. The large area S_Σ (yellow) determines the spacing of the Landau bands, while the small area S_0 and the magnetic breakdown probabilities $T_{\rm MB}$, $T'_{\rm MB}$ determine the band width.

Inspection of figure 3 shows that for $W > W_c$ closed orbits in the interior of the slab coexist with open orbits on the surface. The open and closed orbits are coupled via tunneling through a momentum gap δk_y (MB [25, 26]), with tunnel probability $T_{\rm MB} = 1 - R_{\rm MB}$ given by the Landau–Zener formula

$$T_{\rm MB} = \exp(-B_c/B), \quad B_c \simeq (\hbar/e)\delta k_y^2 \simeq (\hbar\varepsilon/ev_{\rm F})^2. \tag{4.1}$$

In the expression for the breakdown field B_c a numerical prefactor of order unity is omitted [26, 27].

The real-space orbits are illustrated in figure 4: an electron in a Fermi arc on the top surface switches to the bottom surface when the Fermi arc terminates at a Weyl point [16]. The direction of propagation (helicity) of the surface electron may change as a consequence of the MB, which couples a right-moving electron on the top surface to a left-moving electron on the bottom surface. This backscattering process occurs with reflection probability

$$\mathcal{R} = \left|\frac{T_{\rm MB}}{1 - R_{\rm MB}e^{i\phi}}\right|^2 = \frac{T_{\rm MB}^2}{T_{\rm MB}^2 + 4R_{\rm MB}\,\sin^2(\phi/2)}. \tag{4.2}$$

The phase shift ϕ accumulated in one round trip along the closed orbit is determined by the enclosed area S_0 in momentum space,

$$\phi = S_0 l_m^2 + 2\pi\nu, \tag{4.3}$$

with $\nu \in [0, 1)$ a magnetic-field independent offset.

Resonant tunneling through the closed orbit, resulting in $\mathcal{R} = 1$, happens when ϕ is an integer multiple of 2π. We thus see that the resonances are periodic in $1/B$, with period

$$\Delta(1/B) = \frac{2\pi e}{\hbar S_0} \approx \frac{e}{\hbar}(W/W_c - 1)^{-3/2}k_{\rm F}^{-2}. \tag{4.4}$$

(We have substituted the small-ε expression (3.9) for S_0.)

The Shubnikov–de Haas (SdH) oscillations due to Landau level quantisation are also periodic in $1/B$. Their period is determined by the area $S_\Sigma \approx 2\pi k_{\rm F}/a_0$ in figure 5, hence

$$\Delta(1/B)_{\rm SdH} = \frac{2\pi e}{\hbar S_\Sigma} \approx \frac{ea_0}{\hbar k_{\rm F}}. \tag{4.5}$$

Comparison with equation (4.4) shows that the period of the SdH oscillations is smaller than that of the MB oscillations by a factor $k_{\rm F}a_0(W/W_c - 1)^{3/2}$, which is typically $\ll 1$.

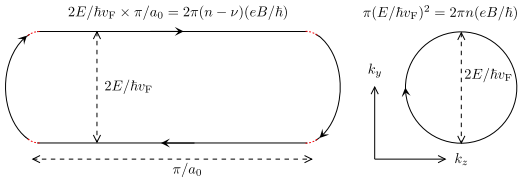

Figure 6. Equi-energy contours in the k_y–k_z plane for surface Fermi arcs coupled by magnetic breakdown (left panel, schematic) and for the bulk cyclotron orbit of a Weyl fermion (right panel). The quantization condition for the enclosed area is indicated, to explain why the Landau level spacing is $\propto B$ for the Fermi arcs, while it is $\propto\sqrt{B}$ for the cyclotron orbit.

5. Dispersive Landau bands

Let us now discuss how MB converts the flat dispersionless Landau levels into dispersive bands. The mechanism crucially relies on the fact that the surface Fermi arcs in a Kramers–Weyl semimetal connect Weyl points at TRIM. Consider two TRIM $\boldsymbol{K}$ and $\boldsymbol{K}'$ in the (k_y, k_z) plane of the surface Brillouin zone. We choose $\boldsymbol{K} = (0, 0)$ at the zone center and $\boldsymbol{K}' = (0, \pi/a_0)$ at the zone boundary, with $\boldsymbol{G} = (0, 2\pi/a_0)$ a reciprocal lattice vector.

In the periodic zone scheme, the Weyl points can be repeated along the k_z-axis with period $2\pi/a_0$, to form an infinite one-dimensional chain (see figure 5). The perpendicular magnetic field B induces a flow along this chain in momentum space, which in real space is oriented along the y-axis with period

$$\mathcal{L} = (2\pi/a_0)l_m^2 = 2\pi v_y/\omega_c, \quad \omega_c = eBv_y a_0/\hbar. \tag{5.1}$$

In the weak-field regime $l_m \gg a_0$ the period $\mathcal{L}$ of the magnetic-field induced superlattice is large compared to the period a_0 of the atomic lattice. We seek the band structure of the superlattice.

We distinguish the Weyl points at $\boldsymbol{K}$ and $\boldsymbol{K}'$ by their different MB probabilities, denoted respectively by $T_{\rm MB} = 1 - R_{\rm MB}$ and $T'_{\rm MB} = 1 - R'_{\rm MB}$. We focus on the case that $T_{\rm MB}$ and $T'_{\rm MB}$ are close to unity and the areas S_0 and S'_0 of the closed orbits are the same—this is the small-ε regime in equations (3.9) and (4.1). (The more general case is treated in appendix C.)

The phase shift ψ accumulated upon propagation from one Weyl point to the next is gauge dependent, we choose the Landau gauge $\boldsymbol{A} = (0, -Bz, 0)$. For simplicity we ignore the curvature of the open orbits, approximating them by straight contours along the line $k_y = E/\hbar v_y$. The phase shift is then given by

$$\psi = \frac{E}{\hbar v_y}\frac{\pi}{a_0}l_m^2 = \frac{\pi E}{\hbar\omega_c}, \tag{5.2}$$

the same for each segment of an open orbit connecting two Weyl points.

The quantization condition for a Landau level at energy E_n is $2\psi + \phi = 2\pi n$, $n = 1, 2, \ldots$, which amounts to the quantization in units of h/e of the magnetic flux through the real-space area $S_\Sigma l_m^4$. Since $S_\Sigma \gg S_0$ the Landau level spacing is governed by the energy dependence of ψ,

$$E_{n+1} - E_n \approx \pi(\mathrm{d}\psi/\mathrm{d}E)^{-1} = \hbar\omega_c. \tag{5.3}$$

The Landau level spacing increases $\propto B$ and not $\propto\sqrt{B}$, as one might have expected for massless electrons. The origin of the difference is explained in figure 6.

The Landau levels are flat when $T_{\rm MB} = T'_{\rm MB} = 1$, so that there are no open orbits. The open orbits introduce a dispersion along k_y, see figure 7. Full expressions are given in appendix C. For $R_{\rm MB}, R'_{\rm MB} \ll 1$ and $S_0 = S'_0$ we have the dispersion

$$E(k_y) = (n-\nu)\hbar\omega_c \pm (\hbar\omega_c/\pi)\sin(\phi/2)\left(R_{\rm MB} + R'_{\rm MB} + 2\sqrt{R_{\rm MB}R'_{\rm MB}}\,\cos\,k_y\mathcal{L}\right)^{1/2}, \tag{5.4}$$

where the phase ϕ is to be evaluated at $E = (n-\nu)\hbar\omega_c$.

Each Landau level is split into two subbands having the same band width

$$|E(0) - E(\pi/\mathcal{L})| = 2\left(\hbar\omega_c/\pi\right)|\sin\left(\phi/2\right)|\min\left(\sqrt{R}_{\rm MB}, \sqrt{R'}_{\rm MB}\right). \tag{5.5}$$

The band width oscillates periodically in $1/B$ with period (4.4).

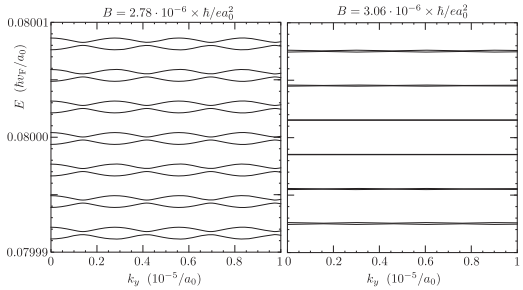

Figure 7. Dispersion relation of the slab in a perpendicular magnetic field B, calculated from equations (C5) and (C6) (for $W = 20a_0$, $T_{\rm MB} = 0.85$, $T'_{\rm MB} = 0.95$, $S_0 = S'_0$, $\nu = 0$). In the left panel B is chosen such that the phase ϕ accumulated by a closed orbit at $E = 0.08\hbar v_{\rm F}/a_0$ equals 11π, in the right panel $\phi = 10\pi$. When ϕ is an integer multiple of 2π the magnetic breakdown is resonant, all orbits are closed and the Landau bands are dispersionless. When ϕ is a half-integer multiple of 2π the magnetic breakdown is suppressed and the Landau bands acquire a dispersion from the open orbits.

6. Magnetoconductance oscillations

The dispersive Landau bands leave observable signatures in electrical conduction, in the form of magnetoconductance oscillations due to the resonant coupling of closed and open orbits. These have been previously studied when the open orbits are caused by an electrostatic superlattice [11–15]. We apply that theory to our setting.

From the dispersion relation (5.4) we calculate the square of the group velocity $\mathcal{V} = \partial E/\hbar\partial k_y$, averaged over the Landau band,

$$\begin{aligned}\langle \mathcal{V}^2\rangle &= \frac{\mathcal{L}}{2\pi}\int_0^{2\pi/\mathcal{L}} \left(\frac{{\rm d}E(k_y)}{\hbar\ {\rm d}k_y}\right)^2 {\rm d}k_y \\ &= 2v_y^2\ \sin^2(\phi/2)\ \min(R_{\rm MB}, R'_{\rm MB}).\end{aligned} \tag{6.1}$$

For weak impurity scattering, scattering rate $1/\tau_{\rm imp} \ll \omega_{\rm c}$, the effective diffusion coefficient [15],

$$D_{\rm eff} = \tau_{\rm imp}\langle \mathcal{V}^2\rangle, \tag{6.2}$$

and the 2D density of states $N_{\rm 2D} = (\pi\hbar v_y a_0)^{-1}$ of the Landau band, determine the oscillatory contribution $\delta\sigma_{yy}$ to the longitudinal conductivity via the Drude formula for a 2D electron gas,

$$\begin{aligned}\delta\sigma_{yy} &= e^2 N_{\rm 2D} D_{\rm eff} \\ &= \frac{4e^2}{h}\frac{v_y\tau_{\rm imp}}{a_0}\ \sin^2(\phi/2)\ \min(R_{\rm MB}, R'_{\rm MB}).\end{aligned} \tag{6.3}$$

The magnetoconductance oscillations due to MB coexist with the SdH oscillations due to Landau level quantization. Both are periodic in $1/B$, but with very different period, see equations (4.4) and (4.5).

At zero temperature the amplitudes of the MB and SdH oscillations are comparable, both of the order of the zero-field conductivity $\sigma_0 = e^2 N_{\rm 2D} v_{\rm F}^2 \tau_{\rm imp}$. But the difference in period causes a very different temperature dependence, which allows to distinguish the two types of magnetoconductance oscillations.

A conductance measurement at temperature T corresponds to an energy average over a range $\Delta E \approx 4k_{\rm B}T$ (being the full-width-at-half-maximum of the derivative of the Fermi–Dirac distribution). The oscillations become unobservable when the energy average changes the area S_0 or S_Σ by more than π/l_m^2. This results in different characteristic energy or temperature scales,

$$\Delta E_{\rm SdH} = \frac{\pi}{l_m^2}\left(\frac{\partial S_\Sigma}{\partial E}\right)^{-1} \simeq \frac{1}{2}\hbar\omega_{\rm c}, \tag{6.4a}$$

$$\Delta E_{\rm MB} = \frac{\pi}{l_m^2}\left(\frac{\partial S_0}{\partial E}\right)^{-1} \simeq \frac{1}{4}\sqrt{2}(W/W_{\rm c} - 1)^{-1/2}\frac{\hbar\omega_{\rm c}}{k_{\rm F}a_0}. \tag{6.4b}$$

(In the second equation we took $W/W_{\rm c} \gtrsim 1$.) For $k_{\rm F}a_0 \ll 1$ and $W/W_{\rm c}$ close to unity we may have $\Delta E_{\rm SdH} \ll \Delta E_{\rm MB}$, so there is an intermediate temperature regime $\Delta E_{\rm SdH} \lesssim 4k_{\rm B}T \lesssim \Delta E_{\rm MB}$ where the SdH oscillations are suppressed while the MB oscillations remain.

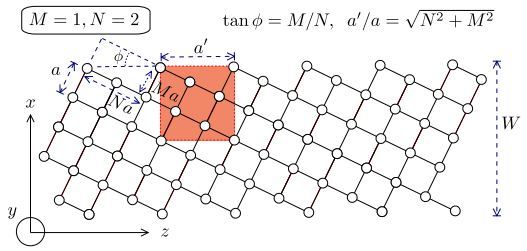

Figure 8. Slice at $y = 0$ through the cubic lattice, rotated around the y-axis by an angle $\phi = \arctan(M/N)$ with $M = 1, N = 2$. The enlarged unit cell (red square), parallel to a lattice termination at $x = 0$ and $x = W$, has volume $a' \times a' \times a = (N^2 + M^2)a^3$.

The condition $W/W_c \gtrsim 1$ is essential for the visibility of the MB oscillations. If W drops below W_c the slab has only open orbits and the resonant tunneling into closed orbits disappears. If on the contrary W becomes much larger than W_c, then the MB oscillations vanish because of thermal averaging while the SdH oscillations are still largely unaffected.

7. Tight-binding model on a cubic lattice

We have tested the analytical calculations from the previous sections numerically, on a tight-binding model of a Kramers–Weyl semimetal [1]. In this section we describe the model, results are presented in the next section.

For this numerical study we take isotropic Kramers–Weyl cones for simplicity, the generalization to anisotropic cones is given in the analytical part. Note that time-reversal symmetry forbids a spin-independent term linear in momentum, which implies that unlike generic Weyl cones the Kramers–Weyl cones cannot be tilted in momentum space [1].

7.1. Hamiltonian

We take a simple cubic lattice (lattice constant a, one atom per unit cell), when the nearest-neighbor hopping terms are the same in each direction $\alpha \in \{x, y, z\}$. There are two terms to consider, a spin-independent term $\propto t_0$ that is even in momentum and a spin–orbit coupling term $\propto t_1\sigma_\alpha$ that is odd in momentum,

$$H = t_0 \sum_\alpha \cos(k_\alpha a) + t_1 \sum_\alpha \sigma_\alpha \sin(k_\alpha a) - t_0. \tag{7.1}$$

The offset is arbitrarily fixed at $-t_0$.

There are 8 Weyl points (momenta $\boldsymbol{k}$ in the Brillouin zone of a linear dispersion), located at $k_x, k_y, k_z \in \{0, \pi\}$ modulo 2π. The Weyl points at $(k_x, k_y, k_z) = (0,0,0), (\pi,\pi,0), (\pi,0,\pi), (0,\pi,\pi)$ have positive chirality and those at $(\pi,\pi,\pi), (\pi,0,0), (0,\pi,0), (0,0,\pi)$ have negative chirality [1].

The geometry is a slab, with a normal $\hat{n}$ in the x–z plane at an angle ϕ with the x-axis (so the normal is rotated by ϕ around the y-axis). The boundaries of the slab are constructed by removing all sites at $x < 0$ and $x > W$. In the rotated basis aligned with the normal to the slab one has

$$\begin{pmatrix} k_x' \\ k_z' \end{pmatrix} = \begin{pmatrix} \cos\phi & \sin\phi \\ -\sin\phi & \cos\phi \end{pmatrix} \begin{pmatrix} k_x \\ k_z \end{pmatrix}, \quad k_y' = k_y. \tag{7.2}$$

We will work in this rotated basis and for ease of notation omit the prime, writing k_x or $k_\perp$ for the momentum component perpendicular to the slab and $(k_y, k_z) = \boldsymbol{k}_\parallel$ for the parallel momenta.

7.2. Folded Brillouin zone

The termination of the lattice in the slab geometry breaks the translation invariance in the perpendicular x-direction as well as in the z-direction parallel to the surface. If the rotation angle $\phi \in (0, \pi/2]$ is chosen such that $\tan\phi = M/N$ is a rational number (M and N being coprime integers), the translational invariance in the z-direction is restored with a larger lattice constant $a' = a\sqrt{N^2 + M^2}$, see figure 8. There are then $N^2 + M^2$ atoms in a unit cell.

In reciprocal space the enlarged unit cell folds the Brillouin zone. Relative to the original Brillouin zone the folded Brillouin zone is rotated by an angle ϕ around the y-axis and scaled by a factor $(N^2 + M^2)^{-1/2}$ in the x and z-directions, see figure 9. The reciprocal lattice vectors in the rotated basis are

$$\boldsymbol{e}_x = (2\pi/a')\hat{x}, \quad \boldsymbol{e}_y = (2\pi/a)\hat{y}, \quad \boldsymbol{e}_z = (2\pi/a')\hat{z}. \tag{7.3}$$

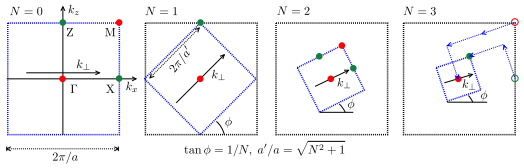

Figure 9. Slice at $k_y = 0$ through the Brillouin zone of the rotated cubic lattice, for rotation angles $\phi = \arctan(M/N)$ with $M = 1$, $N = 0, 1, 2, 3$. Weyl points of opposite chirality are marked by a green or red dot. The panel for $N = 3$ shows how translation by reciprocal lattice vectors (blue arrows) folds two Weyl points onto each other.

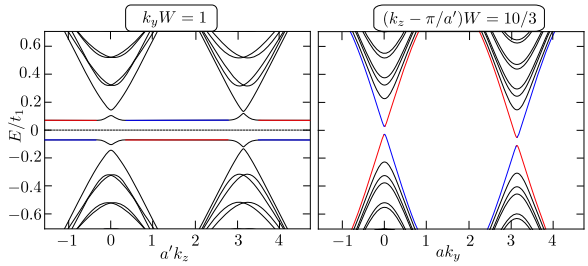

Figure 10. Dispersion relations of a slab (thickness $W = 10\sqrt{2}\,a$ in the x-direction, infinitely extended in the y–z plane) in zero magnetic field. The plots are calculated from the tight-binding model of section 8 (with $t_0 = 0.04t_1$, $\delta t_0 = -0.02t_1$, corresponding to $\varepsilon = 0.06t_1$, $\varepsilon' = 0.02t_1$). The left and right panels show the dispersion as a function of k_z and k_y, respectively. The curves are colored according to the electron density on the surfaces: red for the bottom surface, blue for the top surface, with bulk states appearing black.

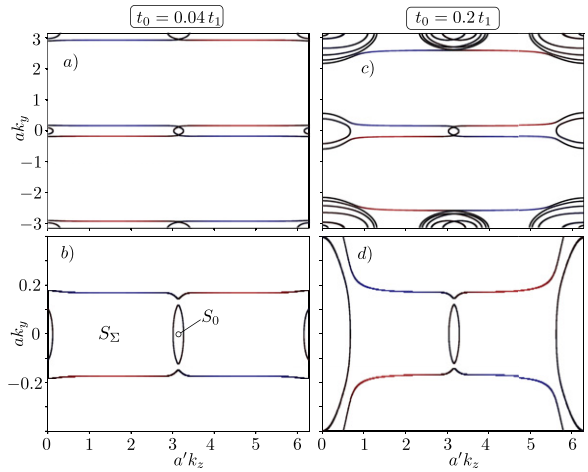

Figure 11. Panels (a) (full Brillouin zone) and (b) (zoom-in near $k_y = 0$) show equi-energy contours at $E = 0.167t_1$ (when $W \approx 1.5W_c$), for the same system as in figure 10. In panels (c) and (d) the spin-independent hopping term t_0 is increased by a factor 5 (at the same $\delta t_0 = -0.02t_1$).

The corner in the $k_y = 0$ plane of the original Brillouin zone (the M point) has coordinates

$$\frac{\pi}{a}(\cos\ \phi + \sin\ \phi, \cos\ \phi - \sin\ \phi, 0) = \frac{\pi}{a'}(N + M, N - M, 0)$$

in the rotated lattice. Upon translation over a reciprocal lattice vector this is folded onto the center of the Brillouin zone (the Γ point) when $N + M$ is an even integer, while it remains at a corner for $N + M$ odd. The midpoints of a zone boundary, the X and Z points, are folded similarly, as summarized by

$$M \mapsto \Gamma, \Gamma \mapsto \Gamma, X \mapsto M, Z \mapsto M, \quad \text{for } N + M \text{ even},$$

$$M \mapsto M, \Gamma \mapsto \Gamma, X \mapsto X, Z \mapsto Z, \quad \text{for } N + M \text{ odd}.$$

Since the Weyl points at Γ and M have the same chirality, for $N + M$ even we are in the situation that the surface of the slab couples Weyl points of the same chirality—which is required for surface Fermi arcs

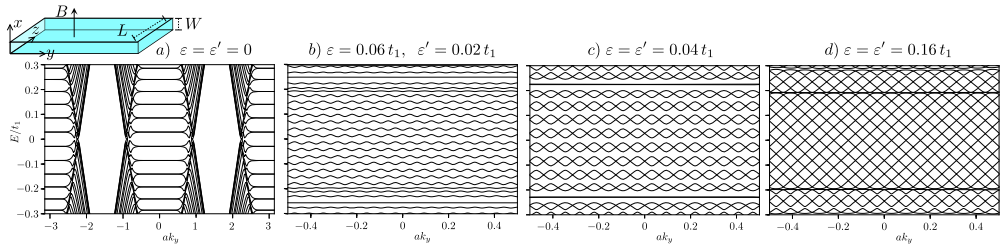

Figure 12. Dispersion relation of a strip (cross-section $W \times L$ with $W = 10a'$ and $L = 30a'$) in a perpendicular magnetic field $B = 0.007\,07(h/ea^2)$ (magnetic length $l_m = 4.74a$). The four panels correspond to $t_0/t_1, \delta t_0/t_1$ equal to 0, 0 [panel (a)], 0.04, −0.02 [panel (b)], 0.04, −0.04 [panel (c)], 0.16, −0.16 [panel (d)]. The surface Fermi arcs near $k_y = 0$ form closed orbits in panel (a), producing flat Landau levels, while in panel (d) they form open orbits with the same linear dispersion as in zero field. Panels (b) and (c) show an intermediate regime where magnetic breakdown between closed and open orbits produces Landau bands with an oscillatory dispersion.

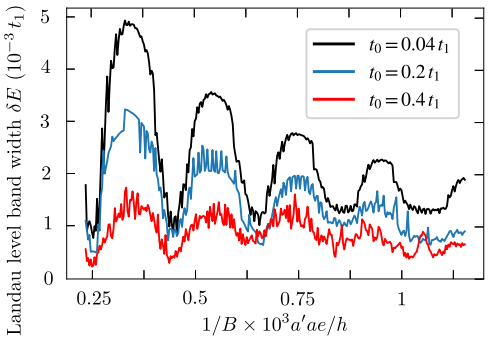

Figure 13. Band width of the Landau levels versus inverse of magnetic field for $W = 10a'$, $L = 500a'$, $\delta t_0 = -0.02t_1$ and three different values of t_0. The band widths are averaged over an energy window $\Delta E = 0.004t_1$ around the Fermi energy $E_F = 0.167t_1$. The rapid SdH oscillations are averaged out, only the slow oscillations due to magnetic breakdown persist.

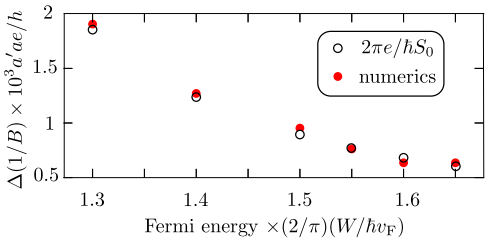

Figure 14. Periodicity in $1/B$ of the Landau band width oscillations as a function of the Fermi energy, for $W = 10a'$, $L = 500a'$, $t_0 = 0.04t_1$, and $\delta t_0 = -0.02t_1$. The filled data points are obtained numerically from the Landau band spectrum, similarly to the data shown for one particular E_F in figure 13. The open circles are calculated from the area S_0 of the closed orbit in momentum space (as indicated in figure 11(b)), using the formula $\Delta(1/B) = 2\pi e/\hbar S_0$.

to appear (see section 2). For $N + M$ odd, in contrast, the Weyl points at the Γ and X points of opposite chirality are coupled by the surface, since these line up along the $k_\perp$ axis. Then surface Fermi arcs will not appear. In appendix B we present a general analysis, for arbitrary Bravais lattices, that determines which lattice terminations support Fermi arcs and which do not.

8. Tight-binding model results

We present results for $M = N = 1$, corresponding to a $\phi = \pi/4$ rotation of the lattice around the y-axis. The folded and rotated Brillouin zone has a pair of Weyl points of + chirality at $\boldsymbol{K} = (0, 0, 0)$ and a second pair of − chirality at $\boldsymbol{K}' = (\pi/a', 0, \pi/a')$ in the rotated coordinates (see figure 9, second panel, with $a' = a\sqrt{2}$). There is a second pair translated by $k_y = \pi/a$.

Each Weyl point supports a pair of Weyl cones of the same chirality, folded onto each other in the first Brillouin zone. The Weyl cones at $\boldsymbol{K}$ have energy offset $\varepsilon = |2t_0|$, while those at $\boldsymbol{K}'$ have $\varepsilon' = 0$. We may adjust the offset by adding a rotational symmetry breaking term $\delta H = \delta t_0 \cos k_z\, a$ to the tight-binding

Hamiltonian (7.1). This changes the offsets into

$$\varepsilon = |2t_0 + \delta t_0|, \quad \varepsilon' = |\delta t_0|. \tag{8.1}$$

In figure 10 we show how the Fermi arcs appear in the dispersion relation connecting the Weyl cones at $k_z = 0$ and $k_z = \pi/a'$. This figure extends the local description near a Weyl cone from figure 2 to the entire Brillouin zone. The corresponding equi-energy contours are presented in figure 11. Increasing the spin-independent hopping term t_0 introduces more bands, but the qualitative picture near the center of the Brillouin zone remains the same as in figure 3 for $W > W_c$.

The effect on the dispersion of a magnetic field B, perpendicular to the slab, is shown in figure 12 (see also appendix D). The field was incorporated in the tight-binding model via the Peierls substitution in the gauge $\boldsymbol{A} = (0, -Bz, 0)$, with coordinate z restricted to $|z| < L/2$. Translational invariance in the y-direction is maintained, so we have a one-dimensional dispersion $E(k_y)$. The boundaries of the system at $z = \pm L/2$ introduce edge modes, which are visible in panel (a) as linearly dispersing modes near $k_y = \pm\frac{1}{2}L/l_m^2$ (modulo π/a). Panels (b)–(d) focus on the region near $k_y = 0$, where these edge effects can be neglected. The effect on the dispersion of a variation in ε and ε' is qualitatively similar to that obtained from the analytical solution of the continuum model, compare the four panels of figure 12 with the corresponding panels in figure 16.

The width δE of the dispersive Landau bands (from maximum to minimum energy) is plotted as a function of $1/B$ in figure 13 and the periodicity $\Delta(1/B)$ is compared with the predicted equation (4.4) in figure 14. To remove the rapid SdH oscillations we averaged over an energy interval ΔE around E_F. This corresponds to a thermal average at effective temperature $T_{\text{eff}} = \Delta E/4k_B$. From equation (6.4), with $k_F a \approx 0.2$, $W/W_c \approx 1.5$, we estimate that the characteristic energy scale at which the oscillations average out is five times smaller for the SdH oscillations than for the oscillations due to MB, consistent with what we see in the numerics.

9. Conclusion

In conclusion, we have shown that Kramers–Weyl fermions (massless fermions near TRIM) confined to a thin slab have a fundamentally different Landau level spectrum than generic massless electrons: the Landau levels are not flat but broadened with a band width that oscillates periodically in $1/B$. The origin of the dispersion is MB at Weyl points, which couples open orbits from surface Fermi arcs to closed orbits in the interior of the slab.

The band width oscillations are observable as a slow modulation of the conductance with magnetic field, on which the rapid SdH oscillations are superimposed. The periodicities are widely separated because the quantized areas in the Brillouin zone are very different (compare the areas S_0 and S_Σ in figure 5). This is a robust feature of the band structure of a Kramers–Weyl semimetal, as illustrated in the model calculation of figure 11. Since generic Weyl fermions have only the SdH oscillations, the observation of two distinct periodicities in the magnetoconductance would provide for a unique signature of Kramers–Weyl fermions. Such an observation would require a significant advance in materials science, recent progress in the realization of Weyl semimetal thin films is a promising step in that direction [29].

The dispersive Landau band is interpreted as the band structure of a one-dimensional superlattice of MB centra, separated in real space by a distance $\mathcal{L} = (eBa_0/h)^{-1}$—which in weak fields is much larger than the atomic lattice constant a_0. Such a MB lattice has been studied in the past for massive electrons [26], the Kramers–Weyl semimetals would provide an opportunity to investigate their properties for massless electrons.

Acknowledgments

The tight-binding model calculations were performed using the Kwant code [30]. This project has received funding from the Netherlands Organization for Scientific Research (NWO/OCW) and from the European Research Council (ERC) under the European Union's Horizon 2020 research and innovation programme.

Appendix A. Coupling of time-reversally invariant momenta by the boundary

The derivation of the boundary condition for Kramers–Weyl fermions in section 2 relies on pairwise coupling of Weyl cones at a TRIM by the boundary. Let us demonstrate that this is indeed what happens.

Consider a 3D Bravais lattice and its Brillouin zone. A time-reversally-invariant momentum (TRIM) is by definition a momentum $\boldsymbol{K}$ such that $\boldsymbol{K} = -\boldsymbol{K} + \boldsymbol{G}$ with $\boldsymbol{G}$ a reciprocal lattice vector, or equivalently,

$\boldsymbol{K} = \frac{1}{2}\boldsymbol{G}$. Now consider the restriction of the lattice to $x > 0$, by removing all lattice points at $x < 0$. Assume that the restricted lattice is still periodic in the y–z plane, with an enlarged unit cell. Figure 8 shows an example for a cubic lattice.

The enlarged unit cell will correspond to a reduced Brillouin zone, with a new set of reciprocal lattice vectors $\tilde{\boldsymbol{G}}$. The original set $\boldsymbol{K}_1, \boldsymbol{K}_2, \boldsymbol{K}_3, \ldots$ of TRIM is folded onto a new set $\tilde{\boldsymbol{K}}_1, \tilde{\boldsymbol{K}}_2, \tilde{\boldsymbol{K}}_3, \ldots$ in the reduced Brillouin zone. The folding may introduce degeneracies, such that two different $\boldsymbol{K}$'s are folded onto the same $\tilde{\boldsymbol{K}}$. The statement to prove is this:

- Each TRIM $\tilde{\boldsymbol{K}}$ in the folded Brillouin zone is either degenerate (because two $\boldsymbol{K}$'s were folded onto the same $\tilde{\boldsymbol{K}}$), or there is a second TRIM $\tilde{\boldsymbol{K}}'$ along the k_x-axis.

Figure 9 illustrates that this statement is true for the cubic lattice. We wish to prove that it holds for any Bravais lattice.

Enlargement of the unit cell changes the primitive lattice vectors from $\boldsymbol{a}_1, \boldsymbol{a}_2, \boldsymbol{a}_3$ into $\tilde{\boldsymbol{a}}_1, \tilde{\boldsymbol{a}}_2, \tilde{\boldsymbol{a}}_3$. The two sets are related by integer coefficients n_{ij},

$$\tilde{\boldsymbol{a}}_i = \sum_{j=1}^{3} n_{ij}\boldsymbol{a}_j, \quad n_{ij} \in \mathbb{Z}. \tag{A1}$$

The corresponding primitive vectors $\boldsymbol{b}$, $\tilde{\boldsymbol{b}}$ in reciprocal space satisfy

$$\boldsymbol{b}_i \cdot \boldsymbol{a}_j = 2\pi\delta_{ij}, \quad \tilde{\boldsymbol{b}}_i \cdot \tilde{\boldsymbol{a}}_j = 2\pi\delta_{ij}. \tag{A2}$$

Any momentum $\boldsymbol{k}$ can thus be expanded as

$$\boldsymbol{k} = \frac{1}{2\pi}\sum_{i=1}^{3} (\tilde{\boldsymbol{a}}_i \cdot \boldsymbol{k})\tilde{\boldsymbol{b}}_i = \frac{1}{2\pi}\sum_{i,j=1}^{3} n_{ij}(\boldsymbol{a}_j \cdot \boldsymbol{k})\tilde{\boldsymbol{b}}_i. \tag{A3}$$

A TRIM $\boldsymbol{K}_\alpha$ in the first Brillouin zone of the original lattice is given by

$$\boldsymbol{K}_\alpha = \frac{1}{2}\sum_{i=1}^{3} m_{\alpha,i}\boldsymbol{b}_i, \quad m_{\alpha,i} \in \{0, 1\}. \tag{A4}$$

The index α labels each TRIM, identified by the 8 distinct triples $(m_{\alpha,1}, m_{\alpha,2}, m_{\alpha,3}) \in \mathbb{Z}_2 \otimes \mathbb{Z}_2 \otimes \mathbb{Z}_2$. Subsitution into the expansion (A3) gives

$$\begin{aligned}\boldsymbol{K}_\alpha &= \frac{1}{2}\sum_{l=1}^{3} m_{\alpha,l}\left(\frac{1}{2\pi}\sum_{i,j=1}^{3} n_{ij}(\boldsymbol{a}_j \cdot \boldsymbol{b}_l)\tilde{\boldsymbol{b}}_i\right) \\ &= \frac{1}{2}\sum_{i,j=1}^{3} m_{\alpha,j}n_{ij}\tilde{\boldsymbol{b}}_i.\end{aligned} \tag{A5}$$

We now fold $\boldsymbol{K}_\alpha \mapsto \tilde{\boldsymbol{K}}_\alpha$ into the first Brillouin zone of the $\tilde{\boldsymbol{b}}$ reciprocal vectors,

$$\begin{aligned}\tilde{\boldsymbol{K}}_\alpha &= \sum_{i=1}^{3} \nu_{\alpha,i}\tilde{\boldsymbol{b}}_i, \quad \nu_{\alpha,i} \in [0, 1)\,, \\ \nu_{\alpha,i} &= \frac{1}{2}\sum_{j=1}^{3} m_{\alpha,j}n_{ij} \pmod 1.\end{aligned} \tag{A6}$$

In table 1 we list for each TRIM and each choice of $(n_{i1}, n_{i2}, n_{i3}) \in \mathbb{Z}_2 \otimes \mathbb{Z}_2 \otimes \mathbb{Z}_2$ the corresponding value of $\nu_{\alpha,i} \in \{0, \frac{1}{2}\}$.

We fix the y and z-components of $\tilde{\boldsymbol{K}}_\alpha$ by specifying $\nu_{\alpha,2}$ and $\nu_{\alpha,3} \in \{0, \frac{1}{2}\}$ and ask how many choices of α remain, so how many values of α satisfy the two equations

$$\begin{aligned}\nu_{\alpha,2} &= \frac{1}{2}\sum_{i=1}^{3} n_{2i}m_{\alpha,i} \pmod 1, \\ \nu_{\alpha,3} &= \frac{1}{2}\sum_{i=1}^{3} n_{3i}m_{\alpha,i} \pmod 1.\end{aligned} \tag{A7}$$

Inspection of table 1 shows that the number of solutions is even. More specifically, there are

Table 1. Values of $\nu_{\alpha,i}$ calculated from equation (A6), for each triple $n_{i1}n_{i2}n_{i3}$ and each triple $m_{\alpha,1}m_{\alpha,2}m_{\alpha,3}$ (both $\in \mathbb{Z}_2 \otimes \mathbb{Z}_2 \otimes \mathbb{Z}_2$). If we select any two rows and intersect with any column to obtain an ordered pair of values ν, ν', we can then find a second column with the same ν, ν' at the intersection.

	$m_{\alpha,1}m_{\alpha,2}m_{\alpha,3}$							
$n_{i1}n_{i2}n_{i3}$ (mod 2)	000	001	010	011	100	101	110	111
000	0	0	0	0	0	0	0	0
001	0	$\frac{1}{2}$	0	$\frac{1}{2}$	0	$\frac{1}{2}$	0	$\frac{1}{2}$
010	0	0	$\frac{1}{2}$	$\frac{1}{2}$	0	0	$\frac{1}{2}$	$\frac{1}{2}$
011	0	$\frac{1}{2}$	$\frac{1}{2}$	0	0	$\frac{1}{2}$	$\frac{1}{2}$	0
100	0	0	0	0	$\frac{1}{2}$	$\frac{1}{2}$	$\frac{1}{2}$	$\frac{1}{2}$
101	0	$\frac{1}{2}$	0	$\frac{1}{2}$	$\frac{1}{2}$	0	$\frac{1}{2}$	0
110	0	0	$\frac{1}{2}$	$\frac{1}{2}$	$\frac{1}{2}$	$\frac{1}{2}$	0	0
111	0	$\frac{1}{2}$	$\frac{1}{2}$	0	$\frac{1}{2}$	0	0	$\frac{1}{2}$

Table 2. Number of pairs of opposite-chirality Weyl cones that are coupled by a surface termination characterized by the integers $n_{2i}, n_{3i}, i \in \{1, 2, 3\}$. When this number equals 0 the surface couples only Weyl cones of the same chirality and surface Fermi arcs will appear. If the number is different from zero the surface does not support Fermi arcs.

	$n_{31}n_{32}n_{33}$ (mod 2)							
$n_{21}n_{22}n_{23}$ (mod 2)	000	001	010	011	100	101	110	111
000	4	2	2	2	2	2	2	0
001	2	2	1	1	1	1	0	0
010	2	1	2	1	1	0	1	0
011	2	1	1	2	0	1	1	0
100	2	1	1	0	2	1	1	0
101	2	1	0	1	1	2	1	0
110	2	0	1	1	1	1	2	0
111	0	0	0	0	0	0	0	0

- 8 solutions if n_{21}, n_{22}, n_{23} and n_{31}, n_{32}, n_{33} both equal 000 mod 2;
- 4 solutions if only one of n_{21}, n_{22}, n_{23} and n_{31}, n_{32}, n_{33} equals 000 mod 2;
- 4 solutions if n_{21}, n_{22}, n_{23} and n_{31}, n_{32}, n_{33} are identical and different from 000 mod 2;
- 2 solutions otherwise.

The multiple solutions correspond to pairs $\boldsymbol{K}_\alpha$ and $\boldsymbol{K}_\beta$ that are either folded onto the same $\tilde{\boldsymbol{K}}_\alpha = \tilde{\boldsymbol{K}}_\beta$ (if det$n = 0$ mod 2), or onto $\tilde{\boldsymbol{K}}_\alpha$ and $\tilde{\boldsymbol{K}}_\beta$ that differ only in the x-component (if det$n = 1$ mod 2). These are the TRIM that are coupled by the boundary normal to the x-axis.

Appendix B. Criterion for the appearance of surface Fermi arcs

When the boundary couples only Weyl cones of the same chirality, these persist and give rise to surface Fermi arcs. If, however, opposite chiralities are coupled, then the boundary gaps out the Weyl cones and no Fermi arcs appear. Which of these two possibilities is realized can be determined by using that the parity of $m_{\alpha 1} + m_{\alpha 2} + m_{\alpha 3}$ determines the chirality of the Weyl cone at $\boldsymbol{K}_\alpha$.

Table 2 identifies for each choice of n_{21}, n_{22}, n_{33} and n_{31}, n_{32}, n_{33} how many pairs of Weyl cones of opposite chirality are folded onto the same point of the surface Brillouin zone. We conclude that surface Fermi arcs appear if either

- $n_{2i} + n_{3i} = 1$ mod 2 for each i, or
- $n_{21}, n_{22}, n_{23} = 111$ mod 2, or
- $n_{31}, n_{32}, n_{33} = 111$ mod 2.

Appendix C. Calculation of the dispersive Landau bands due to the coupling of open and closed orbits

To calculate the effect of the coupling of open and closed orbits on the Landau levels we apply the scattering theory of references [15, 26, 28] to the equi-energy contours shown in figure 15. We distinguish the two Weyl points at $k_z = 0$ and $k_z = \pi/a_0$ by their different MB probability, denoted respectively by

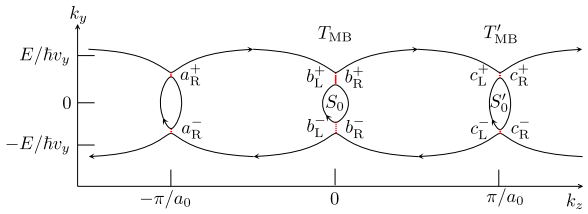

Figure 15. Equi-energy contours in the k_y–k_z plane. The labeled wave amplitudes are related by the scattering and transfer matrices (C1)–(C4).

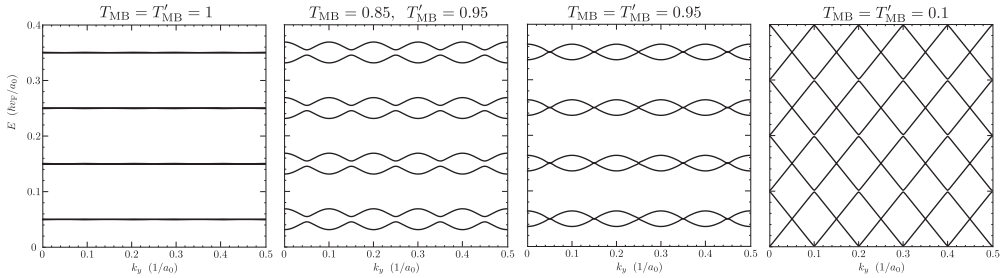

Figure 16. Dispersion relation of the slab in a perpendicular magnetic field, calculated from equations (C5) and (C6) for $W = 1.8a_0$, $S_0 = S'_0$, $\nu = 1/2$, $B = 0.1\,\hbar/ea_0^2$. The four panels correspond to different choices of the magnetic breakdown probabilities $T_{\rm MB}$ and $T'_{\rm MB}$ at the two Weyl points. At the two extremes of strong and weak magnetic breakdown we see dispersionless Landau levels (left-most panel) and linearly dispersing surface modes (right-most panel).

$T_{\rm MB} = 1 - R_{\rm MB}$ and $T'_{\rm MB} = 1 - R'_{\rm MB}$. The areas of the closed orbits may also differ, we denote these by S_0 and S'_0 and the corresponding phase shifts by $\phi = S_0 l_m^2 + 2\pi\nu$ and $\phi' = S'_0 l_m^2 + 2\pi\nu$.

The coupling of the closed and open orbits at these two Weyl points is described by a pair of scattering matrices, given by

$$\begin{pmatrix} b_{\rm L}^- \\ b_{\rm R}^+ \end{pmatrix} = \begin{pmatrix} r & t \\ t & r \end{pmatrix} \cdot \begin{pmatrix} b_{\rm L}^+ \\ b_{\rm R}^- \end{pmatrix}, \quad r = \frac{T_{\rm MB} e^{i\phi/2}}{1 - R_{\rm MB} e^{i\phi}}, \tag{C1a}$$

$$t = -\sqrt{R}_{\rm MB} + \frac{T_{\rm MB}\sqrt{R}_{\rm MB} e^{i\phi}}{1 - R_{\rm MB} e^{i\phi}}, \tag{C1b}$$

for the Weyl point at $k_z = 0$, and similarly for the other Weyl point at $k_z = \pi/a_0$ (with $T_{\rm MB} \mapsto T'_{\rm MB}$, $\phi \mapsto \phi'$). The coefficients can be rearranged in an energy-dependent transfer matrix,

$$\begin{pmatrix} b_{\rm R}^+ \\ b_{\rm R}^- \end{pmatrix} = \mathcal{T}(E) \begin{pmatrix} b_{\rm L}^+ \\ b_{\rm L}^- \end{pmatrix}, \quad \mathcal{T} = \begin{pmatrix} t - r^2/t & r/t \\ -r/t & 1/t \end{pmatrix}, \tag{C2}$$

and similarly for $\mathcal{T}'$ (with $t \mapsto t'$, $r \mapsto r'$). The transfer matrices are energy dependent via the energy dependence of S_0 and hence of ϕ.

We ignore the curvature of the open orbits, approximating them by straight contours along the line $k_y = E/\hbar v_y$. The phase shift accumulated upon propagation from one Weyl point to the next, in the Landau gauge $\boldsymbol{A} = (0, -Bz, 0)$, is then given by

$$\psi = \frac{E}{\hbar v_y}\frac{\pi}{a_0} l_m^2 = \frac{\pi E}{\hbar\omega_{\rm c}}, \quad \omega_{\rm c} = eBv_y a_0/\hbar. \tag{C3}$$

The full transfer matrix over the first Brillouin zone takes the form

$$\begin{pmatrix} c_{\rm R}^+ \\ c_{\rm R}^- \end{pmatrix} = \mathcal{T}_{\rm total}(E) \begin{pmatrix} a_{\rm R}^+ \\ a_{\rm R}^- \end{pmatrix}, \quad \mathcal{T}_{\rm total} = \begin{pmatrix} t' - r'^2/t' & r'/t' \\ -r'/t' & 1/t' \end{pmatrix} \begin{pmatrix} e^{i\psi} & 0 \\ 0 & e^{-i\psi} \end{pmatrix} \begin{pmatrix} t - r^2/t & r/t \\ -r/t & 1/t \end{pmatrix} \begin{pmatrix} e^{i\psi} & 0 \\ 0 & e^{-i\psi} \end{pmatrix}, \tag{C4}$$

$$\mathrm{tr}\ \mathcal{T}_{\rm total} = \frac{\left(e^{i\phi} - R_{\rm MB}\right)\left(e^{i\phi'} - R'_{\rm MB}\right) + \left(1 - e^{i\phi}R_{\rm MB}\right)\left(1 - e^{i\phi'}R'_{\rm MB}\right) - 2T_{\rm MB}T'_{\rm MB}e^{\frac{1}{2}i(\phi+\phi')+2i\psi}}{e^{2i\psi}\left(e^{i\phi} - 1\right)\left(e^{i\phi'} - 1\right)\sqrt{R_{\rm MB}R'_{\rm MB}}}. \tag{C5}$$

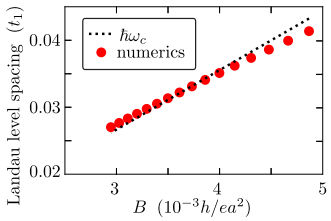

Figure 17. Magnetic field dependence of the energy spacing of the Landau levels near $E = 0$. The numerical data is for the slab geometry of figure 12 ($W = 11a'$, $L = 30a'$) at $t_0 = \delta t_0 = 0$ so that the probability of magnetic breakdown is unity and the Landau levels are dispersionless. The predicted energy spacing $\hbar\omega_c = eBv_F a'$ is the black dotted line.

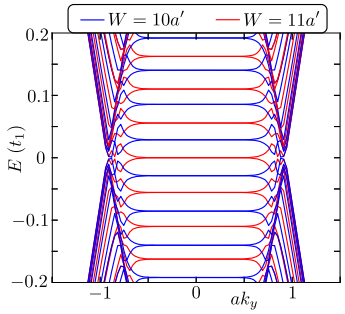

Figure 18. Dispersion relation of the tight-binding model with $t_0 = \delta t_0 = 0$, for $B = 7.07 \times 10^{-3}\ h/ea^2$, $L = 30a'$, and two values of $W = 10a'$ and $11a'$. The Landau levels are shifted by half a level spacing when W/a' switches from odd to even, indicating a shift of the offset ν from 0 to 1/2.

Because det $\mathcal{T}_{\rm total} = 1$, the eigenvalues of $\mathcal{T}_{\rm total}$ come in inverse pairs $\lambda, 1/\lambda$. The transfer matrix translates the wave function over a period $\mathcal{L}$ in real space, so we require that $\lambda = \mathrm{e}^{iq\mathcal{L}}$ for some real wave number q, hence $\lambda + 1/\lambda = \mathrm{e}^{iq\mathcal{L}} + \mathrm{e}^{-iq\mathcal{L}}$, or equivalently [28]

$$\mathrm{tr}\ \mathcal{T}_{\rm total}(E) = 2\ \cos\ q\mathcal{L}. \tag{C6}$$

(In the main text we denote q by k_y, here we choose a different symbol as a reminder that q is a conserved quantity, while the zero-field wave vector is not.) A numerical solution of equation (C6) is shown in figures 7 and 16.

For $T_{\rm MB}$ and $T'_{\rm MB}$ close to unity an analytical solution $E_n(q)$ for the dispersive Landau bands can be obtained. We substitute $\psi = \pi(n-\nu) - (\phi + \phi')/4 + \pi\delta E/\hbar\omega_c$ into equation (C5) and expand to second order in δE and to first order in $R_{\rm MB}, R'_{\rm MB}$. Then we equate to 2 cos $q\mathcal{L}$ to arrive at

$$E_n^{\pm}(q) = (n-\nu)\hbar\omega_c \pm \delta E(q), \tag{C7a}$$

$$(\pi\delta E/\hbar\omega_c)^2 = \rho + \rho' + 2\sqrt{\rho\rho'}\ \cos\ q\mathcal{L}, \tag{C7b}$$

$$\rho = R_{\rm MB}\ \sin^2(\phi/2), \quad \rho' = R'_{\rm MB}\ \sin^2(\phi'/2), \tag{C7c}$$

where ϕ and ϕ' are evaluated at $E = (n-\nu)\hbar\omega_c$. Corrections are of second order in $R_{\rm MB}$ and $R'_{\rm MB}$ and we have assumed that the areas S_0, S'_0 of the closed orbit are small compared to k_F/a_0—so that variations of ϕ and ϕ' over the Landau band can be neglected relative to the band spacing $\hbar\omega_c$.

Appendix D. Landau levels from surface Fermi arcs

As explained in figure 6, the spacing of Landau levels formed out of surface Fermi arcs varies $\propto B$—in contrast to the $\sqrt{B}$ dependence for unconfined massless electrons. In the tight-binding model of section 8 we can test this by setting $\varepsilon = \varepsilon' = 0$, so that there are only closed orbits and the Landau levels are dispersionless. The expected quantization is

$$E_n = (n-\nu)\hbar\omega_c, \quad \omega_c = eBv_F a'/\hbar, \quad n = 0, 1, 2, \ldots \tag{D1}$$

with v_F the velocity in the surface Fermi arc, connecting Weyl points spaced by π/a'. As shown in figure 17, this agrees nicely with the numerics.

In an unconfined 2D electron gas, the offset ν equals 1/2 or 0 for massive or massless electrons, respectively. For the surface Fermi arcs we observe that ν depends on the parity of the number of unit cells between top and bottom surface: $\nu = 0$ if W/a' is odd, while $\nu = 1/2$ if W/a' is even (figure 18). This parity effect suggests that the coupling of Fermi arc states on opposite surfaces, needed to close the orbit in figure 1, introduces a phase shift that depends on the parity of W/a'. We are not aware of such a phase shift for generic Weyl semimetals [16, 17, 31, 32], it seems to be a characteristic feature of Kramers–Weyl fermions that deserves further study.

ORCID iDs

G Lemut https://orcid.org/0000-0002-6946-0035
A Donís Vela https://orcid.org/0000-0002-1627-7245
M J Pacholski https://orcid.org/0000-0002-5245-3517
J Tworzydło https://orcid.org/0000-0003-3410-5460
C W J Beenakker https://orcid.org/0000-0003-4748-4412

References

[1] Chang G *et al* 2018 Topological quantum properties of chiral crystals *Nat. Mater.* **17** 978
[2] Shekhar C 2018 Chirality meets topology *Nat. Mater.* **17** 953
[3] Rao Z *et al* 2019 Observation of unconventional chiral fermions with long Fermi arcs in CoSi *Nature* **567** 496
[4] Sanchez D S *et al* 2019 Topological chiral crystals with helicoid-arc quantum states *Nature* **567** 500
[5] Takane D *et al* 2019 Observation of chiral fermions with a large topological charge and associated Fermi-arc surface states in CoSi *Phys. Rev. Lett.* **122** 076402
[6] Yuan Q-Q *et al* 2019 Quasiparticle interference evidence of the topological Fermi arc states in chiral fermionic semimetal CoSi *Sci. Adv.* **5** eaaw9485
[7] Schröter N B M *et al* 2019 Chiral topological semimetal with multifold band crossings and long Fermi arcs *Nat. Phys.* **15** 759
[8] Zhang C-L *et al* 2017 Ultraquantum magnetoresistance in Kramers–Weyl semimetal candidate β–Ag_2Se *Phys. Rev.* B **96** 165148
[9] Wan B, Schindler F, Wang K, Wu K, Wan X, Neupert T and Lu H-Z 2018 Theory for the negative longitudinal magnetoresistance in the quantum limit of Kramers–Weyl semimetals *J. Phys.: Condens. Matter* **30** 505501
[10] Wen-Yu H, Xu X Y and Law K T 2019 Kramers–Weyl semimetals as quantum solenoids and their applications in spin–orbit torque devices (arXiv:1905.12575)
[11] Gerhardts R R, Weiss D and von Klitzing K 1989 Novel magnetoresistance oscillations in a periodically modulated two-dimensional electron gas *Phys. Rev. Lett.* **62** 1173
[12] Winkler R W, Kotthaus J P and Ploog K 1989 Landau band conductivity in a two-dimensional electron system modulated by an artificial one-dimensional superlattice potential *Phys. Rev. Lett.* **62** 1177
[13] Beenakker C W J 1989 Guiding-center-drift resonance in a periodically modulated two-dimensional electron gas *Phys. Rev. Lett.* **62** 2020
[14] Středa P and MacDonald A H 1990 Magnetic breakdown and magnetoresistance oscillations in a periodically modulated two-dimensional electron gas *Phys. Rev.* B **41** 11892
[15] Gvozdikov V M 2007 Magnetoresistance oscillations in a periodically modulated two-dimensional electron gas: the magnetic-breakdown approach *Phys. Rev.* B **75** 115106
[16] Potter A C, Kimchi I and Vishwanath A 2014 Quantum oscillations from surface Fermi-arcs in Weyl and Dirac semi-metals *Nat. Commun.* **5** 5161
[17] Zhang Y, Bulmash D, Hosur P, Potter A C and Vishwanath A 2016 Quantum oscillations from generic surface Fermi arcs and bulk chiral modes in Weyl semimetals *Sci. Rep.* **6** 23741
[18] Akhmerov A R and Beenakker C W J 2008 Boundary conditions for Dirac fermions on a terminated honeycomb lattice *Phys. Rev.* B **77** 085423
[19] Hasan M Z, Xu S-Y, Belopolski I and Huang S-M 2017 Discovery of Weyl fermion semimetals and topological Fermi arc states *Annu. Rev. Condens. Matter Phys.* **8** 289
[20] Yan B and Felser C 2017 Topological materials: Weyl semimetals *Annu. Rev. Condens. Matter Phys.* **8** 337
[21] Burkov A A 2018 Weyl metals *Annu. Rev. Condens. Matter Phys.* **9** 359
[22] Armitage N P, Mele E J and Vishwanath A 2018 Weyl and Dirac semimetals in three-dimensional solids *Rev. Mod. Phys.* **90** 15001
[23] Bovenzi N, Breitkreiz M, O'Brien T E, Tworzydło J and Beenakker C W J 2018 Twisted Fermi surface of a thin-film Weyl semimetal *New J. Phys.* **20** 023023
[24] Barsan V and Kuncser V 2017 Exact and approximate analytical solutions of Weiss equation of ferromagnetism and their experimental relevance *Phil. Magn. Lett.* **97** 359
[25] Pippard A B 1969 Magnetic breakdown *Physics of Solids in Intense Magnetic Fields* (Berlin: Springer)
[26] Kaganov M I and Slutskin A A 1983 Coherent magnetic breakdown *Phys. Rep.* **98** 189
[27] Stark R W and Falicov L M 1967 Magnetic breakdown in metals *Prog. Low Temp. Phys.* **5** 235
[28] Gvozdikov V M 1986 Thermodynamic oscillations in periodic magnetic breakdown structures *Fiz. Nizk. Temp.* **12** 705
[29] Bedoya-Pinto A *et al* 2020 Realization of epitaxial NbP and TaP Weyl semimetal thin films *ACS Nano* **14** 4405
[30] Groth C W, Wimmer M, Akhmerov A R and Waintal X 2014 Kwant: a software package for quantum transport *New J. Phys.* **16** 063065
[31] Alexandradinata A and Glazman L 2017 Geometric phase and orbital moment in quantization rules for magnetic breakdown *Phys. Rev. Lett.* **119** 256601
[32] Breitkreiz M, Bovenzi N and Tworzydło J 2018 Phase shift of cyclotron orbits at type-I and type-II multi-Weyl nodes *Phys. Rev.* B **98** 121403